

Molecular Dynamics of Organophosphorous Hydrolases Bound to the Nerve Agent Soman

Thereza A. Soares,[†] Mohamed A. Osman,[‡] and T. P. Straatsma^{*,†}

Pacific Northwest National Laboratory, 902 Battelle Blvd., P.O. Box 999 MSIN K7-90,
Richland, Washington 99352, and School of Electrical Engineering and Computer
Science, Washington State University, Pullman, Washington 99164

Received January 25, 2007

Abstract: The organophosphorous hydrolase (OPH) from *Pseudomonas diminuta* is capable of degrading extremely toxic organophosphorous compounds with a high catalytic turnover and broad substrate specificity. Although the natural substrate for OPH is unknown, its triple-mutant H254G/H257W/L303T exhibits a 3 order of magnitude increase in catalytic efficiency and modified stereospecificity toward the most toxic *SpSc* enantiomer of soman. Molecular dynamics simulations and binding free-energy calculations have been undertaken for the wild-type and triple-mutant H254G/H257W/L303T enzymes bound to the *SpSc*-soman enantiomer. Comparison of the simulations indicates that substrate binding induces conformational changes of the loops near the active site. The coordination of the zinc cations in the active site of OPH differs between the free enzyme and the complexes. This suggests that the active site of OPH can accommodate several catalytically active coordination geometries, consistent with the fact that the enzymatic activity of the wild-type OPH can be enhanced by alterations to the metal content of the enzyme. It is also argued that the enhanced efficiency of the triple mutant is determined by enzyme-transition-state complementarity. These results provide a qualitative, molecular-level explanation for the 3 order of magnitude increase in catalytic efficiency of the triple-mutant toward *SpSc*-soman.

Introduction

Organophosphates are extremely toxic chemicals produced by the reaction of alcohols and phosphoric acid. Their biological effect is the inactivation of acetylcholinesterase, which results in the accumulation of the neurotransmitter acetylcholine in the synaptic cleft. In excess, acetylcholine overactivates the postsynaptic receptors and decreases the rate of signal transmission of neurons. Organophosphates are exclusively synthetic compounds that were first developed as insecticides in the 1930s. However, their toxic properties were rapidly identified and further developed as nerve agents during World War II.¹ Soman, also known by its NATO designation GD (O-pinacolyl methylphosphonofluoridate) was the third of the so-called G-series nerve agents to be synthesized [along with GA (tabun), GB (sarin), and GF (cyclosarin)]. The median lethal dose, LC₅₀, is 70 mg min m⁻³ in humans, and its sole application is as a military weapon.^{2–4}

The bacterial enzyme organophosphorous hydrolase (OPH) has been shown to catalyze the cleavage of P–O, P–F, and P–S bonds in a variety of organophosphate triesters and related phosphonates with a high catalytic turnover and broad substrate specificity.^{5–11} Although its natural substrate is unknown, OPH exhibits a turnover of 10⁴ s⁻¹ for the best substrates, while the corresponding values for $k_{\text{cat}}/K_{\text{M}}$ approach the diffusion limit of 10⁸ M⁻¹ s⁻¹.^{12,5} In addition, OPH exhibits stereoselectivity for the hydrolysis of chiral organophosphate triesters, and mutant forms have been engineered with enhanced catalytic activity toward the most toxic stereoisomers of analogs of sarin, soman, and VX.^{7,8,10,11} Among them, the triple-mutant H254G/H257W/L303T exhibits a 3 order of magnitude increase in catalytic efficiency and modified stereospecificity toward the most toxic *SpSc* enantiomer of soman.^{13,14} As a result, catalytically enhanced OPH mutants have a potential application as biosensors for this class of nerve agents, demonstrated by experimental studies in which the immobilization of OPH in nanopores led to enhanced stability and catalytic reaction rates compared to the free enzyme in solution.¹⁵

* Corresponding author. E-mail: tps@pnl.gov.

[†] Pacific Northwest National Laboratory.

[‡] Washington State University.

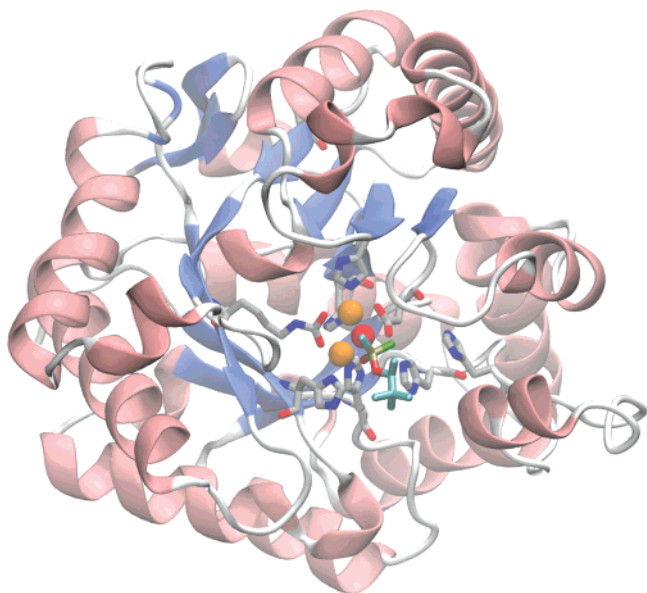


Figure 1. Cartoon representation of the OPH monomer. Active site residues (carbon atoms in gray) and *SpSc*-soman (carbon atoms in cyan) are represented as sticks. Water oxygen atoms (red) and Zn^{2+} cations (orange) are represented in CPK.

X-ray structures have been obtained for the wild-type and mutant forms of OPH complexes with different substrate analogs.^{16–19} These structures reveal a homodimeric (α/β)₈-barrel containing an active site with two divalent metal ions coordinated to the protein through interactions with four histidine and one aspartate residue. The two metal ions are bridged by a water molecule and a carbomoylated lysine residue (Figure 1). Although Zn^{2+} is the native metal ion, substantial activity is observed after substitution by Co^{2+} , Cd^{2+} , Mn^{2+} , or Ni^{2+} .^{5,20} The kinetic constants, k_{cat} and $k_{\text{cat}}/K_{\text{M}}$, are dependent upon the identity of the specific metal cations within the active site. A single-step mechanism has been proposed where the bridging solvent molecule is activated for an in-line $\text{S}_{\text{N}}2$ -nucleophilic attack via complexation to the binuclear metal center and a hydrogen-bonding interaction with residue Asp301.^{8,21}

Enzymatic catalysis is an inherently dynamic process²² in which the binding and release of ligands are often accompanied by conformational changes that may involve large-scale structural rearrangements or local fluctuations in atomic positions.^{23–26} In particular for OPH, kinetic studies have shown that the rate-limiting step of enzymatic hydrolysis appears to involve a conformational change or diffusion-controlled dissociation.⁶ Previous molecular dynamics (MD) simulations suggest that OPH undergoes a substantial conformational change, inducing the opening of a gateway in a pocket where the location of the substrate-leaving group is expected.²⁷ During this rearrangement, Tyr309 was proposed to assist the leaving group, as it exits from the hydrophobic pocket. However, mutational studies of the mutant Y309F failed to find any significant difference in the magnitude of either k_{cat} or $k_{\text{cat}}/K_{\text{M}}$ when compared to those of the wild-type enzyme for the hydrolysis of either paraoxon or a sarin analog.²¹

In order to characterize the contribution of local and global motions to the enhanced activity of the OPH triple-mutant

H254G/H257W/L303T toward *SpSc*-soman, molecular dynamics simulations were performed for OPH wild-type and the complexes of the wild-type/triple-mutant and the substrate *SpSc*-soman. These simulations indicate that substrate binding induces conformational changes of the loops near the active site and that the coordination geometry of the zinc cations in the active site of the enzyme differs between the free enzyme and the complexes. In addition, binding energies of association between wild-type/triple-mutant and the substrate *SpSc*-soman were calculated from a thermodynamic cycle based on continuum electrostatics and a surface-area-dependent nonpolar term. The comparison of calculated and experimentally derived binding energies provides a rationale for the enhanced activity of the triple-mutant enzyme.

Methods

Molecular Systems. MD simulations in explicit solvent were performed for the wild-type (OPH_{wtc}) and triple-mutant (OPH_{tmc}) monomers of the enzyme organophosphorous hydrolase bound to soman and for the unbound wild-type homodimer (OPH_{wt}). Each monomer contains a structurally and catalytically independent active site,^{16–19} and therefore the structural dynamics of the monomers and dimers are expected to be comparable. Initial coordinates were taken from crystallographic structures with PDB entry codes 1EZ2 and 1P6C at 1.9 and 2.0 Å resolution, respectively.¹³ The cocrystallized diisopropylmethyl phosphonate analog present in both structures was replaced by the *SpSc*-soman enantiomer. Amino acid protonation states were assigned accordingly to a pH of 7.0, and hydrogen atoms were generated using the Prepare module of NWChem.²⁸ The zinc ions were treated using a nonbonded model with a formal charge of +2.²⁹ The geometries of the soman and carbamylated Lys169 were fully optimized by using density functional theory, the B3LYP functional, and the DZVP basis set.³⁰ Partial atomic charges for soman and the carbamylated Lys169 were calculated at the Hartree–Fock level with the 6-31G* basis set and restrained electrostatic potential procedure³¹ on the geometry-optimized structures. These charges were used in combination with the AMBER95 force field parameters.³² The structures were solvated in a cubic box with dimensions of 7.4, 7.6, and 10.0 nm³ for OPH_{wtc}, OPH_{tmc}, and OPH_{wt}, respectively. Water molecules within 0.28 nm of any atom in the solute were removed. Periodic boundary conditions and the SPC/E water model³³ were used to describe the solvent molecular interactions.

Molecular Dynamics Simulations. MD simulations were carried out for the NPT ensemble with a time step of 1 fs during the equilibration and 2 fs during the production runs. The temperatures of the solute and solvent were controlled by separately coupling them to a Berendsen thermostat³⁴ with a relaxation time of 0.1 ps. The pressure was maintained at 1.025×10^5 Pa by means of isotropic coordinate scaling with a relaxation time $\tau = 0.4$ ps. A time step of 2 fs was used to integrate the equations of motion on the basis of the leapfrog algorithm.³⁵ The bond lengths between hydrogen and heavy atoms were constrained by using the SHAKE algorithm³⁶ with a tolerance of 10^{-3} nm. A short-range cutoff of 1.0 nm was used for all nonbonded interactions, and long-range electrostatic interactions were treated by the smooth particle mesh Ewald (PME) method.³⁷ The equilibration procedure consisted of thermalization of the solvent, with

the solute atoms fixed, for 20 ps at 298.15 K, followed by minimization of all solute atoms, keeping the solvent coordinates fixed, and then simulation of the complete system by raising the temperature from 0 to 298.15 K in 20 ps increments of 50 K each for MD simulation. Data production was carried out for 5 ns, and configurations of the trajectory were recorded every 0.2 ps. Within the modest simulation times of 5 ns, several structural properties, including backbone root-mean-square-deviation (RMSD), have reached convergence. All simulations were performed with the NWChem program,²⁸ and the analyses of molecular trajectories were carried out using data-intensive trajectory analysis capabilities of the DIANA module.³⁸

Electrostatic Calculations. The free energy of ligand–protein association may be approximated in the form³⁹

$$\Delta G_{\text{bind}} = \Delta G_{\text{elec}} + \Delta G_{\text{np}} - T\Delta S \quad (1)$$

where ΔG_{elec} is the electrostatic contribution, ΔG_{np} is the nonpolar or hydrophobic term, and $-T\Delta S$ describes the change in entropy (conformational, translational, and rotational) upon complexation. The change in flexibility of the enzyme and substrate upon binding is assumed to be similar in the wild type and triple mutant. In this case, the entropic contribution will be the same for the two systems and cancel in the calculation of the relative free energy of binding. The electrostatic term ΔG_{elec} was calculated by solving the linearized Poisson–Boltzmann equation with the Adaptive Poisson–Boltzmann Solver package.⁴⁰ The calculations were performed at 298.15 K and an ionic strength of 0 M. Dielectric constants of 2 and 78 were assigned to the solute and solvent, respectively. The dielectric boundary between the solute and solvent was based on the molecular surface definition calculated with a probe sphere radius of 0.14 nm. For the boundary conditions, the focusing method was applied⁴¹ with multigrid points $65 \times 65 \times 65$, coarse grid lengths $0.33 \times 0.33 \times 0.33 \text{ nm}^3$, and fine grid dimensions $0.16 \times 0.16 \times 0.16 \text{ nm}^3$. The nonpolar term ΔG_{np} is estimated on the basis of the amount of the solvent-accessible surface area buried upon binding

$$\Delta G_{\text{np}} = \gamma \Delta A \quad (2)$$

where ΔA is the change in solvent-accessible surface area upon binding and γ is the apolar constant $0.105 \text{ kJ mol}^{-1} \text{ \AA}^{-2}$. This empirical coefficient (effective microscopic interfacial tension) is calibrated to reproduce experimental transfer free energies of alkane molecules from the liquid alkane phase into water.^{42,43} In order to estimate the relative strength of binding of *SpSc*-soman to the wild-type and triple-mutant forms of OPH, we have applied the above equation to 20 structures sampled at regular time intervals from each of the two MD simulations.

Results and Discussion

Structural Stability and Flexibility of OPH. Atom-positional RMSD and root-mean-square fluctuation (RMSF) were calculated from the MD simulations for OPH_{wtc}, OPH_{tmc}, and OPH_{wt} with respect to the X-ray structures 1EZ2 (wild type) and 1P6C (triple mutant), respectively (Figures 2 and 3). Monomeric and dimeric wild-type ensembles exhibit comparable RMSD values, which converge to 0.1

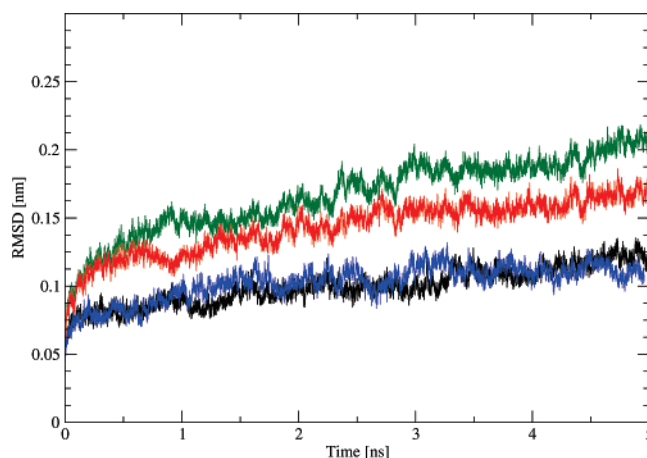


Figure 2. Root-mean-square deviation of the α -carbon atoms of OPH_{wtc} (black), OPH_{tmc} (green), OPH_{tmc} without the loop regions corresponding to residues 260–276 and 305–315 (red), and OPH_{wt} (blue) with respect to the X-ray structures 1EZ2 and 1P6C as described in the text.

nm after a time period of 3 ns. The OPH_{tmc} ensemble exhibits RMSD values of about 0.2 nm. The loop regions corresponding to residues 260–276 and 305–315 are responsible for the slow convergence of the RMSD along the OPH_{tmc} simulation. Convergence is obtained when these residues are excluded from the RMSD calculations (Figure 2). The residues in both loops are involved in large-scale atomic displacement as discussed below. Likewise, atom-position RMSF for the monomeric and dimeric wild-type simulations are very similar (Figure 3). One exception is the region corresponding to residues 60–70, which displays larger flexibility in the OPH_{wtc} and OPH_{tmc} simulations compared to that in OPH_{wt}. The other is the region formed by residues 130–140, which is more flexible in the OPH_{tmc} ensembles than in the X-ray structure 1P6C. These two regions are part of a loop/short-helix/loop motif located away from the active site, at the protein interface between the two monomers. The apparent reason for their increased flexibility is the exposure to the solvent in the monomer simulations. However, the effect of these fluctuations on the overall structure of the monomers is negligible, as shown by the similarity of the secondary structure pattern between the monomeric and dimeric wild-type ensembles of OPH for which only small and localized differences can be observed (Figure 4). Examples of such differences are the β -strand conformation around residues Val198–His201 in OPH_{wtc} and OPH_{tmc} but not in OPH_{wt} and Ile168–Ala171 in OPH_{wt} and OPH_{tmc} but not in OPH_{wtc}. It can thus be assumed that the MD ensemble for the OPH monomers is representative of the ensemble corresponding to their respective dimeric forms.

The RMSF calculated for the MD simulations can be correlated with the isotropic temperature factors (B-factors) from the crystallographic coordinates (Figure 3). The sizes of the B-factors are representative of the amount of disorder present in the crystal on the time scale of the diffraction experiment, which ranges from seconds to days. The divergence between RMSF and B-factors around residues 205 and 240 in the wild-type simulations is likely due to differences in the experiment and simulation time scales or differences between the crystal and solution environments or force-field limitations. Because the solution and crystal

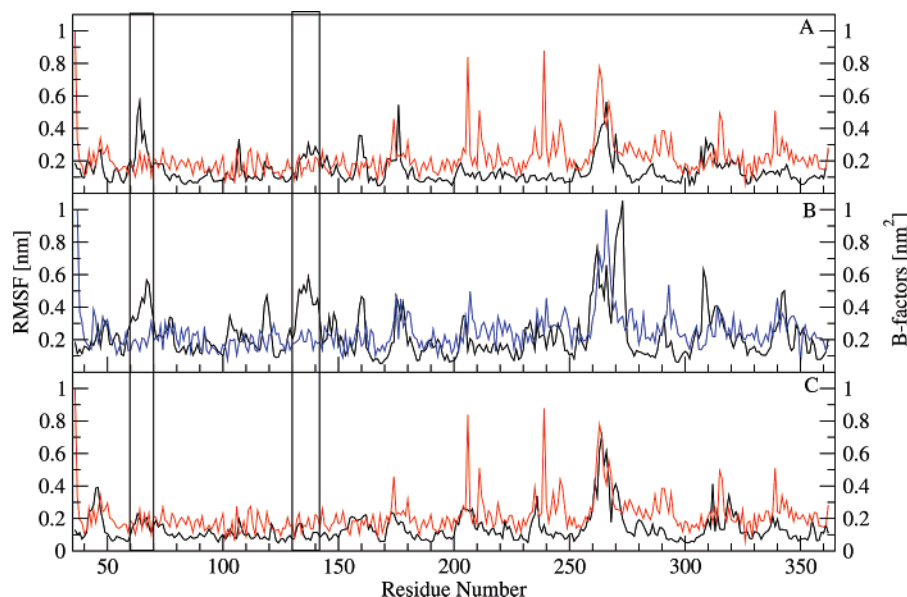


Figure 3. Root-mean-square fluctuations of C_{α} atoms of (A) OPH_{wtc} , (B) OPH_{tmc} , and (C) OPH_{wt} with respect to the X-ray structures 1EZ2 and 1P6C. Isotropic B-factors from the X-ray structures 1EZ2 (red) and 1P6C (blue). The regions highlighted correspond to residues 60–70 and 130–140 discussed in the text.

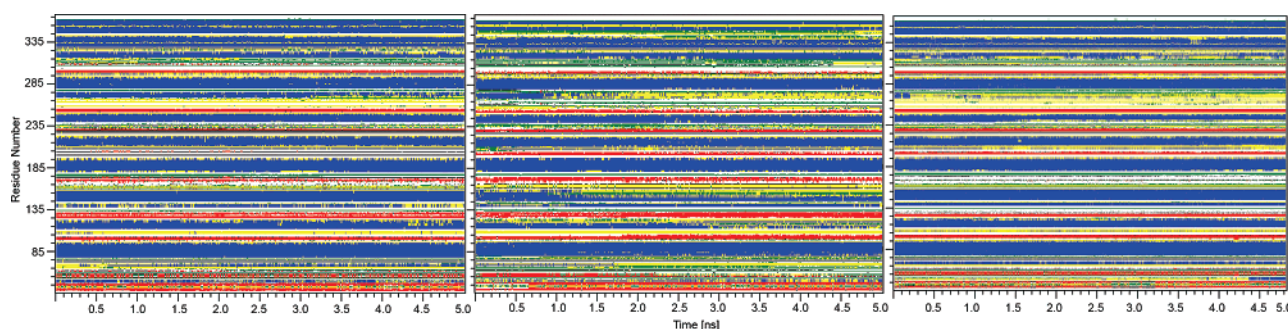


Figure 4. Representation of secondary structure pattern along time for OPH_{wtc} (left), OPH_{tmc} (middle), and OPH_{wt} (right). Color patterns are blue for α -helix, gray for 3-helix, red for β -sheet, black for β -bridge, green for bend, yellow for turn, and white for coil.

environments are different, the comparison of RMSF data from molecular simulations with experimental B-factors should be carried out with caution but can be illustrative to identify common flexible components. In the three simulations, residues 260–270 (260–275 for OPH_{tmc}) exhibit the largest atomic fluctuations. They form a loop/ α -helix motif that, together with seven short loops, delimits the entrance of the active site. In the OPH_{tmc} ensemble, these loops exhibit a discernible atom fluctuation, which is absent in both wild-type ensembles (Figure 3). These results indicate that the mutations H254G, H257W, and L303T alter the internal dynamics of the mutant, leading to an increased flexibility of residues in the entrance of the active site of OPH_{tmc} .

The essential dynamics analysis method was applied to the MD trajectories to separate low-frequency motions that typically determine the kinetics of enzymatic activity from the much larger number of remaining high-frequency motions. This technique is based on a principal component analysis of the positional displacement from an average structure. The separation in low- and high-frequency components is made through a change of coordinate system from Cartesian to these principal components or eigenvectors of the covariance matrix. This method, in principle, allows for the extrapolation of motions in the direction of selected

eigenvectors. In this study, however, this analysis is used to describe the low-frequency, persistent motions observed in the molecular trajectories. The eigenvalue percentages and amplitudes corresponding to the 10 eigenvectors with highest eigenvalues calculated from the OPH_{wtc} , OPH_{tmc} , and OPH_{wt} simulations, respectively, are presented in Table 1. Only a few modes are required to account for the large-amplitude mobility observed in the three ensembles. Most of the large-scale atomic displacement in the OPH_{wtc} and OPH_{tmc} simulations is contained in the first eigenvectors, with eigenvalues of 0.46 and 0.65 nm^2 , respectively. In the OPH_{wt} simulation, the first eigenvector has an eigenvalue of less than 0.23 nm^2 and accounts for 17.9% of the total atom displacement observed in this ensemble.

The contributions of C_{α} atoms to the first and second eigenvectors are presented in Figure 5. They represent the relative displacement of each residue due to the motion described by a given eigenvector. The residues that contribute most to the motions along the first and second eigenvectors in the simulations are confined to the loops in the entrance of the active site. Two regions of the OPH_{wtc} and OPH_{tmc} ensembles exhibit the largest atomic displacements along the first eigenvector: residues 175–180/260–276 and 260–276/305–315, respectively (Figure 5). In the OPH_{wt} ensemble,

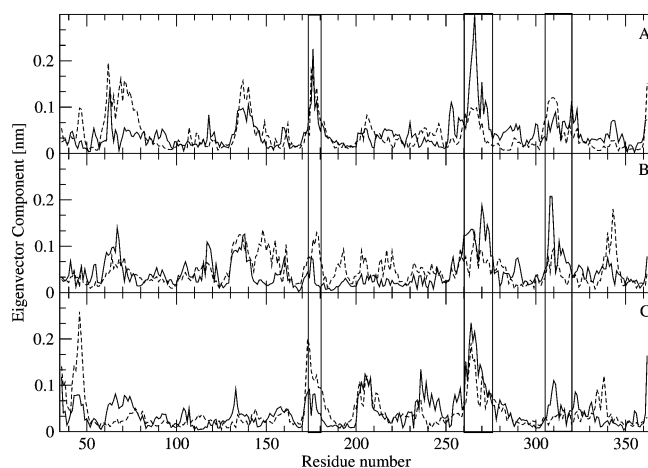


Figure 5. Eigenvector components for atomic displacement along the first (black lines) and second (dashed lines) eigenvectors for the MD-generated ensembles of (A) OPH_{wtc} , (B) OPH_{tmc} , and (C) OPH_{wt} . Residues 175–180 (loop L1), 260–276 (loop L2), and 305–315 (loop L3) are highlighted.

Table 1. Magnitudes of the Eigenvalues Calculated from the Covariance Matrix of α -Carbon Coordinates Corresponding to the MD Simulations OPH_{wtc} , OPH_{tmc} , and OPH_{wt}

eigenvalues	Eigenvalue Magnitudes and Amplitudes		
	magnitude [%]/amplitude [nm ²]		
	OPH_{wtc}	OPH_{tmc}	OPH_{wt}
1	30.85/0.460	30.30/0.650	17.91/0.226
2	6.73/0.100	11.16/0.240	12.58/0.159
3	4.61/0.069	5.18/0.110	5.22/0.066
4	3.79/0.057	3.97/0.085	3.32/0.042
5	2.98/0.045	3.15/0.067	2.94/0.037
6	2.43/0.036	2.52/0.056	2.41/0.034
7	1.91/0.029	2.10/0.045	2.04/0.026
8	1.63/0.024	1.82/0.039	1.84/0.023
9	1.53/0.023	1.58/0.034	1.49/0.09
10	1.36/0.020	1.45/0.031	1.45/0.018

where the substrate soman is absent from the active site, only residues 260–276 contribute significantly to the motion along the first eigenvector. These residues, together with residues 43–50/175–180, also present the largest atom displacement in the motion described by the second eigenvector (eigenvalue of ca. 12.6%) in the OPH_{wt} simulation (Table 1). The loop regions formed by residues 175–180, 260–276, and 305–315 will be referred here as L1, L2, and L3, respectively.

Loops L1 and L2 are located opposite each other across the active site entrance, whereas loops L2 and L3 are located side-by-side. In the motion described by the first eigenvector in the OPH_{wtc} simulation, loops L1 and L2 move in opposite directions from the entrance of the active site (see Figure 6A). In the OPH_{tmc} simulation, a similar motion is observed for loops L2 and L3 also with respect to the active site entrance (Figure 6B). In both ensembles, these displacements lead to a widening of the active site entrance. A qualitative estimate of the width of the opening is given by the distance between residues in loops L1, L2, and L3 and residues located across the active site. The C_α atom distances between L2 residue Ala270 and Phe132, a residue immediately

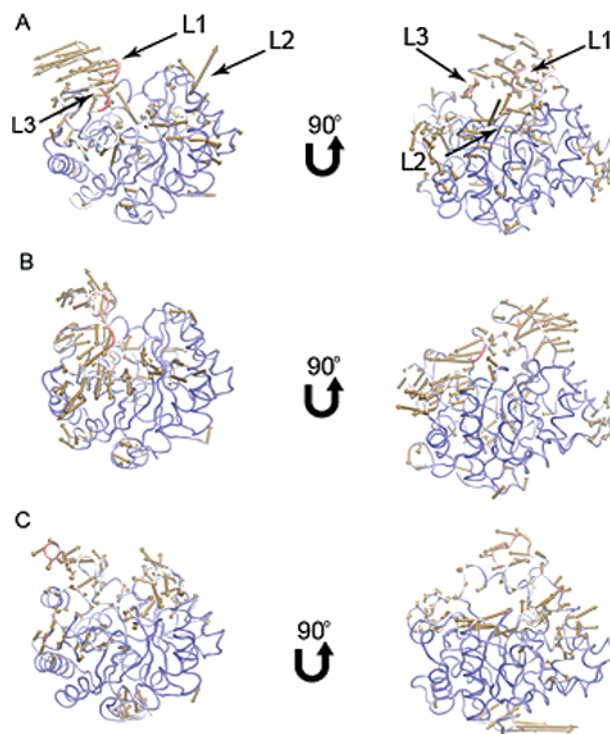


Figure 6. Porcupine plots representing the highest amplitude motions along the first eigenvector for (A) OPH_{wtc} , (B) OPH_{tmc} , and (C) OPH_{wt} . In C, one monomer of the dimer simulation is shown. Only eigenvector components larger than 0.05 ps are shown for clarity. C_α trace colored by atom contribution to the first eigenvector. The color gradient is from red (highest displacement) to blue (lowest displacement). The loop regions L1, L2, and L3 correspond to residues 175–180, 260–276, and 305–315, respectively.

opposite from loop L2 in the direction of the first eigenvector, fluctuates between 1.68 and 2.50 nm. The C_α atom distances between loop L3 residue Ser308 and residue Pro178 opposite this loop fluctuates between 2.36 and 2.56 nm. Similarly for the OPH_{tmc} ensemble, the C_α atom distances between loop L2 residue Ala270 and residue Phe132 is found to be between 1.78 and 2.50 nm, while this distance for loop L3 residue Tyr309 and residue Ser205 fluctuates between 1.72 and 2.32 nm. For OPH_{tmc} , this movement is accompanied by the displacement of Tyr309 toward the active site entrance where its aromatic ring makes hydrophobic contacts with the aliphatic chain of the substrate, reducing solvent access. In the OPH_{wt} ensemble, loop L2 and, to a lesser extent, its neighboring loops display much lower amplitude and less ordered collective displacements along the first eigenvector (Figure 6C). In this ensemble, the distances between the C_α atoms of loop L2 residue Ala270 and residue Phe132 fluctuate between 1.68 and 1.79 nm and those of loop L3 residue Ser308 and residue Pro178 fluctuate between 2.35 and 2.43 nm. These collective motions do not result in any significant conformational rearrangement of residues or displacement of Tyr309 toward the active site entrance of OPH_{wt} , and thus these changes appear to be triggered upon substrate binding.

Binding of *SpSc*-Soman to OPH_{wtc} and OPH_{tmc} . The atom-positional RMSD for the *SpSc*-soman bound to OPH_{wtc} and OPH_{tmc} as a function of time is presented in Figure 7.

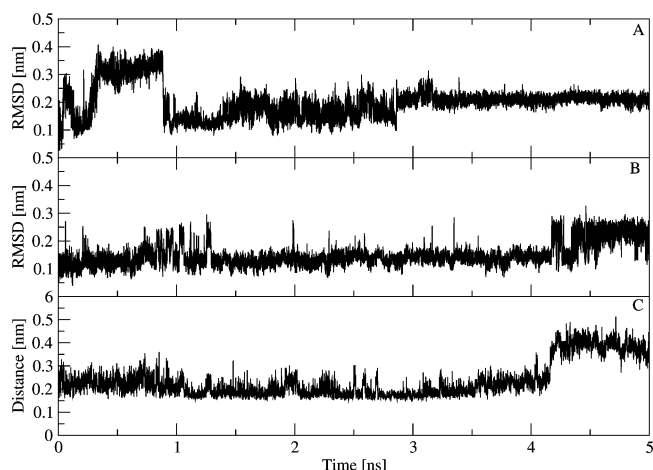


Figure 7. Root-mean-square deviation of the heavy atoms for soman. (A) *SpSc*-soman bound to the wild-type OPH. (B) *SpSc*-soman bound to the triple-mutant OPH. (C) Distance between the phosphoester oxygen atom of *SpSc*-soman and one of the water molecules coordinated to the β -metal in the triple mutant.

In the OPH_{wtc} complex, the substrate undergoes a positional deviation of 0.35 nm from the initial conformation, which subsequently decreases to 0.1–0.15 nm and converges to a plateau around 0.2 nm (Figure 7A). In the OPH_{tmc} complex,

soman exhibits a less fluctuating RMSD pattern around 0.1–0.15 nm during the first 4 ns and then reaches a second plateau around 0.2–0.25 nm (Figure 7B). It also exhibits an average positional fluctuation of 0.21 nm in the OPH_{tmc} complex compared to the corresponding average of 0.25 nm in the OPH_{wtc} complex. This behavior is correlated with a hydrogen bond between the phosphoester oxygen atom of soman and a β -metal-coordinated water molecule that appears to impose a conformational and spatial restraint on the substrate (Figure 7C). This interaction was not observed for the OPH_{wtc} simulation.

The time-dependent behavior of interactions between the nucleophilic water and catalytically important residues was also monitored as shown in Figure 8. The water molecule initially bridging the two cations exhibited an occupancy of 100% in the wild-type ensembles OPH_{wtc} and OPH_{wt} and interacts tightly with the β -metal and with the carboxyl group of Asp301 (Figure 8). In the OPH_{tmc} simulation, this water molecule formed a third interaction with the carbonyl group of Asp253. This hydrogen bond persists for the time simulated, whereas the hydrogen bond between the water molecule and the Asp301 is disrupted after 4 ns. The hydrogen bond between the bridging water molecule and Asp301 is replaced by a new hydrogen bond between the water and His55 imidazole group. One of the water molecules

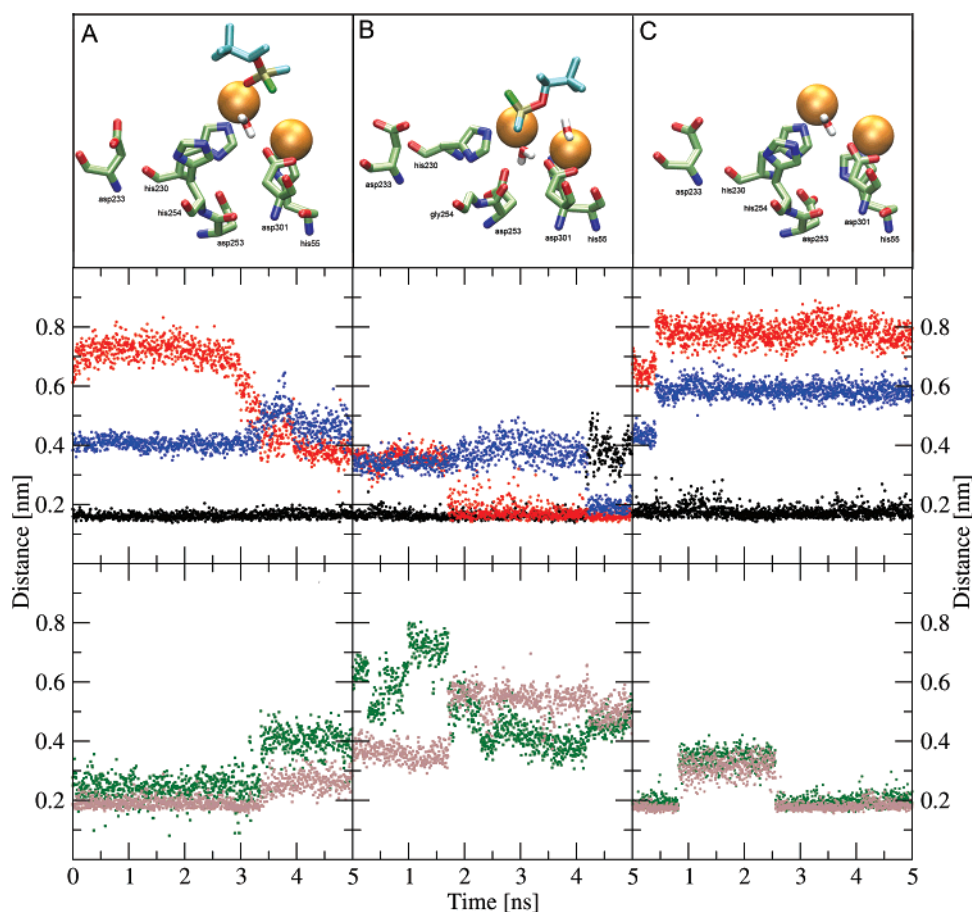


Figure 8. Active site snapshots and distances between catalytic residues and the catalytic water molecule as a function of time. Black circles, Asp301-O δ and water hydrogen atoms; red circles, Asp253-O δ and water hydrogen atoms; blue circles, His55-N ϵ and water hydrogen atoms; green circles, Asp253-O δ and His55-N ϵ atoms; and brown circles, Asp253-O δ and His230-N ϵ atoms. (A) OPH_{wtc}, (B) OPH_{tmc}, and (C) OPH_{wt}. Distances are averaged over 4 ps.

Table 2. Calculated and Experimental^{7,13} Binding Energy Differences for the Complexes Formed by *SpSc*-soman and the Wild-Type and Triple-Mutant H254G/H257W/L303T Forms of OPH

con- formers	Binding Energies ^a [kcal mol ⁻¹]						$\Delta\Delta G_{\text{calc}}$	$\Delta\Delta G_{\text{exp}}^b$
	OPH _{wtc}			OPH _{tmc}				
	ΔG_{elec}	ΔG_{nb}	ΔG_{calc}	ΔG_{elec}	ΔG_{nb}	ΔG_{calc}		
conf.-1	2.71	-11.61	-8.90	3.24	-14.00	-10.76	-3.2	-3.8
conf.-2	4.30	-12.19	-7.89	2.80	-14.55	-11.75		
conf.-3	2.14	-12.20	-10.06	2.86	-14.14	-11.28		
conf.-4	2.70	-11.40	-8.70	3.46	-14.00	-10.54		
conf.-5	4.60	-11.77	-7.17	3.42	-13.94	-10.52		
conf.-6	3.35	-13.30	-9.95	2.99	-13.92	-10.93		
conf.-7	3.01	-12.62	-9.61	0.82	-13.86	-13.04		
conf.-8	2.52	-13.16	-10.64	2.37	-13.99	-11.62		
conf.-9	4.22	-12.60	-8.38	3.74	-13.95	-10.21		
conf.-10	3.19	-13.44	-10.25	4.39	-14.38	-9.99		
conf.-11	3.68	-10.71	-7.03	3.07	-14.07	-11.00		
conf.-12	3.84	-10.54	-6.70	0.27	-14.23	-13.96		
conf.-13	3.85	-10.49	-6.64	2.50	-13.88	-11.38		
conf.-14	4.23	-10.70	-6.47	1.53	-13.71	-12.18		
conf.-15	4.78	-10.73	-5.95	1.14	-14.10	-12.96		
conf.-16	4.87	-12.47	-7.60	1.82	-13.70	-11.88		
conf.-17	3.83	-12.14	-8.31	2.60	-13.63	-11.03		
conf.-18	4.09	-12.15	-8.05	2.12	-13.31	-11.19		
conf.-19	3.62	-12.23	-8.61	1.36	-13.33	-11.97		
conf.-20	5.26	-12.35	-7.09	4.18	-13.58	-9.40		
averages	3.74	-11.94	-8.20	2.53	-13.91	-11.38		

^a $\Delta\Delta G_{\text{calc}}$ is the calculated binding energy difference; ΔG_{elec} and ΔG_{nb} are electrostatics and nonpolar contributions to ΔG_{calc} . ^b $\Delta\Delta G_{\text{exp}}$ is the experimental binding energy difference calculated from $k_{\text{cat}}/K_{\text{M}}^{7,13}$ at 298.15 K and according to $\Delta\Delta G_{\text{exp}} = RT \ln[(k_{\text{cat}}/K_{\text{M}})_{\text{OPH}_{\text{trmc}}}/(k_{\text{cat}}/K_{\text{M}})_{\text{OPH}_{\text{wtc}}}]$.²⁵

coordinated to the β -zinc forms a hydrogen bond with Asp301 and moves to the site earlier occupied by the bridging water molecule. The hydrogen bond between residue Asp253 and the water molecule is possible due to the H254G mutation, which eliminates any potential sterical hindrance by the residue His254 side chain. This interaction is absent in both wild-type simulations regardless of the presence of the substrate soman.

Binding energies between the *SpSc*-soman and the wild-type and triple-mutant forms of OPH were calculated by solving the linearized Poisson–Boltzmann equation in conjunction with a solvent-accessible surface area term for apolar interactions. The calculated binding free energies together with the nonpolar (ΔG_{nb}) and electrostatic (ΔG_{elec}) contributions are presented in Table 2. This model has been shown to overestimate experimental values in part because it does not account for the loss of translational and rotational entropy associated with the binding process. These contributions have been estimated to be 29–63 kJ mol⁻¹ for the binding of small ligands to proteins⁴⁴ and 2–4 kJ mol⁻¹ per frozen (protein or ligand) internal rotational degree of freedom.^{45,46} Therefore, comparisons between calculated and experimental values are presented in terms of differences between the binding energies of the complexes OPH_{wtc} and OPH_{trmc}. A comparison between $\Delta\Delta G_{\text{calc}}$ and $\Delta\Delta G_{\text{exp}}$, where $\Delta\Delta G = \Delta G_{\text{trmc}} - \Delta G_{\text{wtc}}$, shows good agreement between calculated and experimental values since the approximations inherent to the continuum model cancel out. Calculated values indicate that the binding of soman to either the wild-type or the triple-mutant OPH is driven by nonpolar interactions, whereas electrostatics interactions have only a small contribution to the overall binding energy. While this

is true for the thermodynamics of binding of soman to both enzymes, the difference in free energy of binding to the two enzymes, which determines the difference in specificity, has van der Waals and electrostatics contributions of similar magnitude.

The specificity constants $k_{\text{cat}}/K_{\text{M}}$ corresponding to the binding of *SpSc*-soman to the wild-type and triple-mutant enzymes have been determined experimentally.^{7,13} They correspond to values of ca. $1.6 \pm 0.1 \times 10^1$ and 10^4 M⁻¹ s⁻¹, respectively. The specificity constant is a useful quantity to estimate relative binding energies $\Delta\Delta G$ between complexes composed of the same substrate and different enzymes (a parent and a mutant of the parent enzyme) because it accounts for both the activation energy and the binding energy.²⁵ The $\Delta\Delta G_{\text{exp}}$ estimated from experimental values of $k_{\text{cat}}/K_{\text{M}}$ is -15.9 kJ mol⁻¹ more favorable to the binding of *SpSc*-soman to the triple-mutant OPH. Yet, *SpSc*-soman binds to wild-type and triple-mutant enzymes with similar K_{M} values of 2.5 ± 0.5 and 3.1 nM, respectively.^{7,47} The $\Delta\Delta G_{\text{exp}}$ estimated from the experimental values of K_{M} yields a binding energy difference of +0.88 kJ mol⁻¹ less favorable for the complex between *SpSc*-soman and the triple mutant. Therefore, it is the favorable interaction resulting from the enzyme-transition state complementarity—not from the enzyme-substrate complementarity—that makes the triple mutant more efficient than the wild type.

A catalytic mechanism has been proposed for the hydrolysis activity of OPH.^{8,21} In this mechanism, the solvent molecule bridging the two metal ions is activated for an in-line S_N2-nucleophilic attack via complexation to the binuclear metal center and a hydrogen-bonding interaction with residue Asp301.^{8,21} The substrate binds to the active site in an orientation that polarizes the P–O bond of phosphate ester through an interaction of the phosphoryl oxygen with the β -cation. The existence of a bridging water molecule between the two metal ions hydrogen-bonded with Asp301 is observed in both simulations and is consistent with the proposed mechanism. In the context of such a model, we hypothesize that the two hydrogen bonds involving soman and the nucleophilic water, respectively, can enhance the activity of the triple mutant through the stabilization of the transition-state conformation of the substrate. This would happen by means of three effects or their combination: (i) The interactions would force the substrate conformation closer to the transition state structure. (ii) By spatially and conformationally restraining the substrate and the catalytic water with respect to each other, these hydrogen bonds could facilitate the hydrolysis reaction by positioning the substrate and the water molecule in an optimal conformation for the nucleophilic attack. (iii) The negative charge on the trigonal bipyramidal phosphoester of the transition state would be neutralized by the hydrogen bond between the phosphoester oxygen atom of soman and a β -metal coordinated water.

Coordination Number of Zinc Ions in the Active Site.

The active site of OPH contains two Zn²⁺ cations required for full catalytic activity of the enzyme.⁵ In the available crystallographic structures of OPH, the α -metal ion is coordinated to residues His55, His57, and Asp301, while the β -metal ion is coordinated to residues His201 and His230.

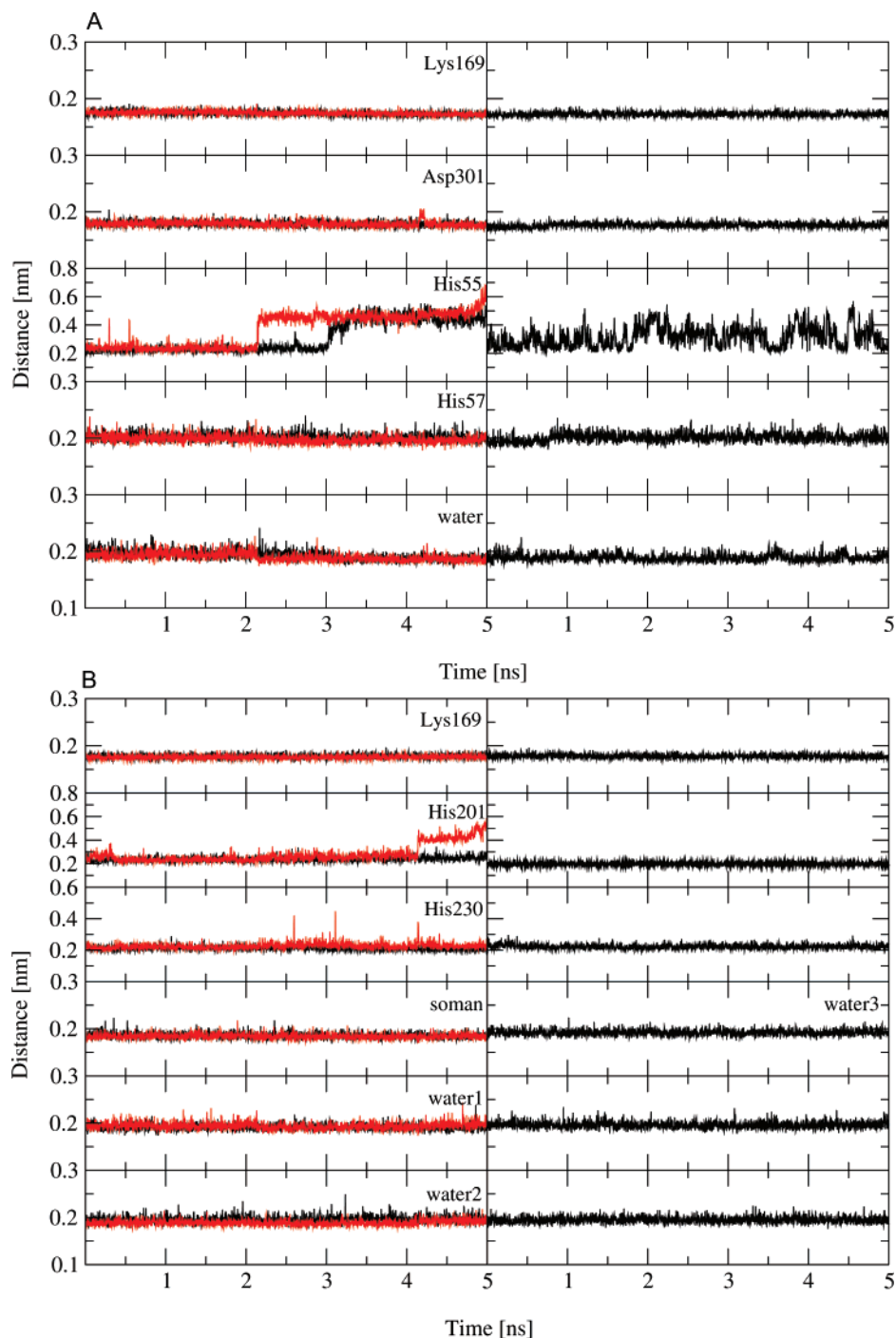


Figure 9. Distances between the Zn^{2+} cations and coordination ligands in the active site of OPH. Left columns: OPH_{wtc} in black and OPH_{tmc} in red. Right columns: OPH_{wt} in black. (A) α -Metal: coordination ligands are the carbamylated residues Lys169, Asp301-O δ , His55-N ϵ , His57-N δ , and one water molecule. (B) β -Metal: coordination ligands are the carbamylated Lys169, His201-N ϵ , His230-N ϵ , soman phosphoryl oxygen atom (only in the OPH_{wtc} in black and OPH_{tmc} simulations on the right), and water molecules.

In addition to these ligands, the two metal ions are bridged via a carboxylated lysine residue and a water molecule, which is thought to be the nucleophile for the hydrolytic attack on the phosphorus atom of the substrate.⁴⁸ The more buried α -metal has a ligand coordination number of five. The β -metal is more solvent-exposed and may acquire additional water ligands. The distances between divalent cations and coordination groups along time for the MD-derived ensembles of OPH are presented in Figure 9A and B.

During the initial 2 ns of simulation, the α -metal maintains a penta-coordinated geometry in the three ensembles (Figure 9). This cation is coordinated to residues His55, His57, and Asp301; the carboxylated Lys169; and a solvent molecule. In the simulations containing the substrate soman, residue His55 moves away from the Zn^{2+} cation, which then adopts a tetra-coordinated geometry. In the OPH_{wt} ensemble, the interaction between residue His55 and the α -metal fluctuates around the range 0.2–0.4 nm. The β -metal is coordinated

to different groups in the three simulations. In the presence of soman, the β -metal binds to the carboxylated residue Lys169, the substrate phosphoryl oxygen, residues His201 and His230, and two water molecules—among which is the nucleophile for the reaction catalyzed by OPH (Figure 9). In the absence of the substrate, a third water molecule replaces the substrate phosphoryl oxygen in the coordination of the metal. The β -metal exhibits predominantly a hexa-coordinated geometry in the MD simulations, but its interaction with His201 is disrupted after 4 ns of simulation in the OPH_{unc} ensemble, leading to a penta-coordinated geometry.

The coordination geometry observed within the simulation times in this study of the α - and β -metals in the MD-derived ensembles can be summarized as follows: (i) in the absence of the substrate, the α -metal is predominantly penta-coordinated; (ii) in the presence of the substrate, the α -metal shifts from penta- to tetra-coordinated after ca. 2–3 ns; (iii) the β -metal is hexa-coordinated in the two wild-type simulations, regardless of the presence of the substrate; (iv) the β -metal transitions from hexa- to penta-coordinated in the OPH_{unc} ensemble after 4 ns of simulation.

Previously, MD simulations of OPH bound to the substrates sarin and paraoxon were carried out by Koça et al.⁴⁹ to examine the coordination number of the Zn^{2+} cations in the protein active site. As in the present work, a nonbonded model²⁹ was employed to treat the Zn^{2+} metals with a charge of +2 in conjunction with the AMBER force field³² and the PME method.³⁷ It was found that such a model could not reproduce the penta-coordinated geometry of the divalent cations observed in the X-ray structures of OPH¹⁸ and obtained by means of ab initio optimization of a model of the active site of OPH composed of the side-chains of a few selected residues.⁴⁹ In these simulations, the less buried β -zinc had a hexa-coordinated geometry, whereas the coordination number of the more buried α -zinc was dependent on the presence of the substrate/inhibitor. In the presence of the substrate, the α -metal was penta-coordinated. Without a substrate, a water molecule was found to move in and bind to the α -metal that became hexa-coordinated. Given that a charge of +1.5 led to a penta-coordinated geometry of both zinc ions, the hexa-coordinated geometry was dismissed as an artifact of the force field used.⁴⁹

The present simulations differ from the study by Koça et al.⁴⁹ in two aspects: the α -zinc does not exhibit hexa-coordination regardless of the presence of the substrate, and the β -zinc is predominantly hexa-coordinated in the three ensembles, although it adopts a penta-coordinated geometry in the OPH_{unc} ensemble after 4 ns. Because the present simulations are at least 5 times longer than the simulations carried out by Koça et al.,⁴⁹ it is possible that the discrepancies between the two studies are due to the different time lengths. However, on the basis of the published X-ray structures of OPH, the claim by Koça et al.⁴⁹ that both Zn^{2+} metals are penta-coordinated appears incorrect. It has been shown that both Zn^{2+} ions in the active site of OPH can be replaced with cadmium or manganese ions without a loss of enzymatic activity.^{5,20} Further examination of the OPH structures currently available in the PDB database shows the more solvent-exposed β -metal with coordination spheres

which are octahedral (in the complexes with $\text{Cd}^{2+}/\text{Cd}^{2+}$, $\text{Mn}^{2+}/\text{Mn}^{2+}$, and $\text{Zn}^{2+}/\text{Cd}^{2+}$),⁵⁰ tetrahedral (in the complex $\text{Zn}^{2+}/\text{Zn}^{2+}$),⁵¹ and trigonal bipyramidal (also in the complex $\text{Zn}^{2+}/\text{Zn}^{2+}$).⁵⁰ In the X-ray structure of the triple mutant, the substitution of His254 with a glycine creates a cavity that allows for the introduction of a third metal binding site.¹³ This third ion, which is absent from the X-ray structure containing a substrate analog, is coordinated in a tetrahedral arrangement by residues Asp253 and His230 and two water molecules, resulting in a distortion of the binuclear center.¹³

The picture emerging from these structural data is that the OPH active site can accommodate several catalytically active coordination geometries. Each of these geometries is possible through the coordination of the metals to additional water ligands or substrate chemical groups. This is consistent with the fact that the enzymatic activity of the wild-type OPH can be enhanced by alterations to the metal content of the enzyme,^{5,52} suggesting that the changes in catalytic metal geometries are associated with the alteration of substrate specificities.^{53,54} Zn^{2+} ions can adopt different numbers of ligands in their first coordination shell, either in solution or as part of metalloproteins,^{55–57} and the energy difference between complexes with different coordination numbers is relatively low.^{58,59} Indeed, much of the ubiquity of Zn^{2+} in functionally diverse proteins has been attributed to its intrinsically flexible coordination geometry.^{55–57,60,61} Furthermore, the solution structure of a protein often differs from its crystal structure due to effects of crystal packing and much lower hydration conditions. In solution, proteins possess a conformational flexibility that includes a wide range of hydration states not seen in the crystal. In addition, although the electron density at the zinc positions in proteins is usually well-defined, the zinc ligation geometry in the X-ray structure may still be influenced by the restraints and parameters used during the refinement procedure. These factors can affect the conformation and position of ligands (side chains and water molecules) around the divalent center, resulting in changes of the metal coordination geometry.

Conclusion

Organophosphorous hydrolase is unique among other organophosphate-degrading enzymes because it can hydrolyze phosphofluoridates, such as soman and sarin, and phosphothioates, such as VX, which constitute the major chemical warfare deterrents stockpiled by the United States and the former Soviet Union. Practical applications of OPH for the detection and detoxification of nerve agents and various environmental pollutants will require enzymes with enhanced structural stability and improved catalytic efficiency. A detailed analysis of the dynamic behavior of wild-type OPH and triple-mutant H254G/H257W/L303T bound to the substrate *SpSc*-soman has been undertaken and compared against the wild-type in the absence of a substrate in an effort to understand how these motions contribute to the enhanced specificity of the mutant. The analyses have shown that, upon substrate binding, OPH undergoes conformational changes that result in the widening of the active site entrance. The conformational changes are mostly limited to the loops in the entrance of the active site and exhibit larger amplitudes

in the triple mutant. These structural rearrangements corroborate previous kinetic studies, indicating that a conformational change might be the rate-limiting step for OPH hydrolysis activity.⁶ It has also been shown that the active site of OPH can accommodate several catalytically active coordination geometries, each of these geometries being possible through the coordination of the metals to additional water ligands or substrate chemical groups. This is consistent with the fact that the enzymatic activity of the wild-type OPH can be enhanced by alterations to the metal content of the enzyme,^{5,52} suggesting that the changes in catalytic metal geometries are associated with the alteration of substrate specificities.^{53,54} Furthermore, the complex between the triple mutant and *SpSc*-soman is stabilized by hydrogen bonds between the phosphoester oxygen atom of soman and a β -metal coordinated water and between the carbonyl group of Asp253 and the catalytic water. This latter interaction is possible only due to the H254G mutation, which eliminates any potential sterical hindrance by the His254 side chain. By spatially and conformationally restraining the substrate and the catalytic water with respect to each other, these hydrogen bonds are expected to facilitate the hydrolysis reaction by positioning the substrate and the water molecule in an optimal conformation for the nucleophilic attack. On the basis of binding energy calculations, we have argued that the enhanced efficiency of the triple mutant is determined by enzyme-transition-state complementarity and not by enzyme-substrate complementarity. Possibly, the hydrogen bonds occurring in the triple-mutant complex stabilize a conformation of the substrate closer to the transition state structure, enhancing the triple mutant specificity.

Acknowledgment. This research was supported by the D.O.E. Office of Advanced Scientific Computing Research. The authors acknowledge the William R. Wiley Environmental Molecular Sciences Laboratory for the computational resources required for this work. T.A.S. and T.P.S. acknowledge Dr. Roberto D. Lins for fruitful discussions. M.A.O. acknowledges Dr. Erich Vorpagel for help with QM calculations. Pacific Northwest National Laboratory is operated for the Department of Energy by Battelle.

References

- Gunderson, C. H.; Lehmann, C. R.; Sidell, F. R.; Jabbari, B. *Neurology* **1992**, *43*, 946–950.
- Brown, M. A.; Brix, K. *J. Appl. Toxicol.* **1998**, *6*, 393–408.
- Lallement, G.; Clarencon, D.; Masqueliez, C.; Baubichon, D.; Galonnier, M.; Burckhart, M.; Peoc'h, M. F.; Mestries, J. C. *Arch. Toxicol.* **1998**, *2*, 84–92.
- Polhuijs, M.; Langenberg, J. P.; Benschop, H. P. *Toxicol. Appl. Pharmacol.* **1997**, *1*, 156–161.
- Omburo, G. A.; Kuo, J. M.; Mullins, L. S.; Raushel, F. M. *J. Biol. Chem.* **1992**, *267*, 13278–13283.
- Caldwell, S. R.; Newcomb, J. R.; Schlechtand, K. A.; Raushel, F. M. *Biochemistry* **1991**, *30*, 7438–7444.
- Li, W. A.; Lum, K. T.; Chen-Goodspeed, M.; Sogorb, M. A.; Raushel, F. M. *Bioorg. Med. Chem.* **2001**, *9*, 2083–2091.
- Li, W. A.; Aubert, S. D.; Raushel, F. M. *J. Am. Chem. Soc.* **2003**, *125*, 7526–7527.
- Chen-Goodspeed, M.; Sogorb, M. A.; Wu, F. Y.; Hong, S. B.; Raushel, F. M. *Biochemistry* **2001**, *40*, 1325–1331.
- Chen-Goodspeed, M.; Sogorb, M. A.; Wu, F. Y.; Raushel, F. M. *Biochemistry* **2001**, *40*, 1332–1339.
- Gopal, S.; Rastogi, V.; Ashman, W.; Mulbry, W. *Biochem. Biophys. Res. Commun.* **2000**, *279*, 516–517.
- Dumas, D. P.; Wild, J. R.; Raushel, F. M. *Experientia* **1990**, *46*, 729–731.
- Hill, C. M.; Li, W. S.; Thoden, J. B.; Holden, M. H.; Raushel, F. M. *J. Am. Chem. Soc.* **2004**, *125*, 8990–8991.
- Benschop, H. P.; Konings, C.; van Genderen, J.; de Jong, L. P. A. *Toxicol. Appl. Pharmacol.* **1984**, *72*, 61–74.
- Lei, C.; Shin, Y.; Liu, J.; Ackerman, E. J. *J. Am. Chem. Soc.* **2002**, *124*, 11242–11243.
- Benning, M. M.; Kuo, J. M.; Raushel, F. M.; Holden, H. *Biochemistry* **1994**, *33*, 15001–15007.
- Benning, M. M.; Kuo, J. M.; Raushel, F. M.; Holden, H. *Biochemistry* **1995**, *34*, 7973–7978.
- Vanhook, J. L.; Benning, M. M.; Raushel, F. M.; Holden, H. M. *Biochemistry* **1996**, *35*, 6020–6025.
- Grimsley, J. K.; Calamini, B.; Wild, J. R.; Mesecar, A. D. *Arch. Biochem. Biophys.* **2005**, *442*, 169–179.
- Rochu, D. N.; Viguié, F. R.; Crouzier, D.; Froment, M. T.; Masson, P. *Biochem. J.* **2004**, *380*, 627–633.
- Aubert, S. D.; Li, Y. C.; Raushel, F. M. *Biochemistry* **1994**, *43*, 5707–5715.
- Boehr, D. D.; Dyson, H. J.; Wright, P. E. *Chem. Rev.* **2006**, *106*, 3055–3079.
- Boehr, D. D.; McElheny, D.; Dyson, H. J.; Wright, P. E. *Science* **2006**, *13*, 1638–1642.
- Schnell, J. R.; Dyson, H. J.; Wright, P. E. *Annu. Rev. Biophys. Biomol. Struct.* **2004**, *33*, 119–140.
- Fersht, A. Enzyme and Substrate Complementarity and Binding Energy. In *Structure and Mechanism in Protein Science: A Guide to Enzyme Catalysis and Protein Folding*; W. H. Freeman: New York, 1998.
- Frauenfelder, H.; Sligar, S. G.; Wolynes, P. G. *Science* **1991**, *254*, 1598–1603.
- Koça, J.; Zhan, C. G.; Rittenhouse, R. C.; Ornstein, R. J. *Am. Chem. Soc.* **2003**, *123*, 817–826.
- Straatsma, T. P. *NWChem, a Computational Chemistry Package for Parallel Computers*, version 4.5; Pacific Northwest National Laboratory: Richland, WA, 2003.
- Stote, R. H.; Karplus, M. *Proteins: Struct., Funct., Genet.* **1995**, *23*, 12–31.
- Godbout, N.; Salahub, D. R.; Andzelm, J.; Wimmer, E. *Can. J. Chem.* **1992**, *70*, 560–571.
- Bayly, C. I.; Cieplak, P.; Cornell, W. D.; Kollman, P. A. *J. Phys. Chem.* **1993**, *97*, 10269–10280.
- Cornell, W. D.; Cieplak, P.; Bayly, C. I.; Gould, I. R.; Merz, K. M.; Ferguson, D. M.; Spellmeyer, D. C.; Fox, T.; Caldwell, W.; Kollman, P. A. *J. Am. Chem. Soc.* **1995**, *117*, 5179–5197.
- Berendsen, H. J. C.; Grigera, J. R.; Straatsma, T. P. *J. Phys. Chem.* **1987**, *91*, 6269–6271.

- (34) Berendsen, H. J. C.; Postma, J. P. M.; van Gunsteren, W. F.; DiNola, A.; Haak, J. R. *J. Chem. Phys.* **1984**, *81*, 3684–3690.
- (35) Hockney, R. W. The Potential Calculation and Some Applications. In *Methods in Computational Physics*; Alder, B., Fernbach, S., Rotenberg, M., Eds.; Academic Press: New York, 1970; Vol. 9.
- (36) Ryckaert, J. P.; Ciccotti, G.; Berendsen, H. J. C. *J. Comput. Phys.* **1977**, *23*, 327–341.
- (37) Essmann, U.; Perera, L.; Berkowitz, M. L.; Darden, T.; Lee, H.; Pedersen, L. G. *J. Chem. Phys.* **1995**, *103*, 8577–8593.
- (38) Straatsma, T. P. *Data Intensive Computing for Complex Biological Systems*; Technical Report 2007, Pacific Northwest National Laboratory: Richland, WA, 2007.
- (39) Froloff, N.; Windemuth, A.; Honig, B. H. *Protein Sci.* **1997**, *6*, 1293–1301.
- (40) Baker, N. A.; Sept, D.; Joseph, S.; Holst, M. J.; McCammon, J. A. *Proc. Natl. Acad. Sci. U.S.A.* **2001**, *98*, 10037–10041.
- (41) Gilson, M. K.; Sharp, K. A.; Honig, B. H. *J. Comput. Chem.* **1988**, *9*, 327–335.
- (42) Simonson, T.; Brünger, A. T. *J. Phys. Chem.* **1994**, *98*, 4683–4694.
- (43) Honig, B. H.; Yang, A. S. *Adv. Protein Chem.* **1995**, *46*, 27–58.
- (44) Gilson, M. K.; Given, J. A.; Bush, B. L.; McCammon, J. A. *Biophys. J.* **1997**, *72*, 1047–1069.
- (45) Doig, A. J.; Sternberg, M. J. E. *Protein Sci.* **1995**, *4*, 2247–2251.
- (46) Janin, J. *Proteins: Struct., Funct., Genet.* **1995**, *21*, 30–39.
- (47) Raushel, F. M. Personal communication, 2006.
- (48) Samples, C. R.; Howard, T.; Raushel, F. M.; DeRose, V. J. *Biochemistry* **2005**, *44*, 11005–11013.
- (49) Koça, J.; Zhan, C. G.; Rittenhouse, R. C.; Ornstein, R. L. *J. Comput. Chem.* **2003**, *24*, 368–378.
- (50) Benning, M. M.; Shim, H.; Raushel, F. M.; Holden, H. M. *Biochemistry* **1998**, *40*, 2712–2722.
- (51) Benning, M. M.; Hong, S. B.; Raushel, F. M.; Holden, H. M. *J. Biol. Chem.* **2000**, *275*, 30556–30560.
- (52) Hong, S. B.; Raushel, F. M. *Biochemistry* **1996**, *35*, 10904–10912.
- (53) Grimsley, J. K.; Scholtz, J. M.; Pacehand, C. N.; Wild, J. R. *Biochemistry* **1997**, *36*, 14366–14374.
- (54) Di-Sioudi, B. D.; Miller, C. E.; Lai, K.; Grimsley, J. K.; Wild, J. R. *Chem. Biol. Interact.* **1999**, *14*, 211–223.
- (55) Alberts, I. L.; Nadassy, K.; Wodak, S. J. *Protein Sci.* **1998**, *7*, 1700–1716.
- (56) Dudev, T.; Lim, C. *Chem. Rev.* **2003**, *103*, 773–787.
- (57) Wang, M. D. J.; Dudev, T.; Lim, C. *J. Phys. Chem. B* **2006**, *110*, 1889–1895.
- (58) Bock, C. W.; Katz, A. K.; Glusker, J. P. *J. Am. Chem. Soc.* **1995**, *117*, 3754–3765.
- (59) Dudev, T.; Lim, C. *J. Am. Chem. Soc.* **2000**, *122*, 11146–11153.
- (60) Lipscomb, W. N.; Strater, N. *Chem. Rev.* **1996**, *96*, 2375–2433.
- (61) Christianson, D. W.; Cox, J. D. *Annu. Rev. Biochem.* **1999**, *68*, 33–57.

CT700024H